J. Fluid Mech. (2104), *vol.* 740, *pp.* 97–113. © Cambridge University Press 2104
doi:10.1017/jfm.2013.645

Two-layer gap-leaping oceanic boundary currents: experimental investigation

Joseph J. Kuehl† and V. A. Sheremet

Graduate School of Oceanography, University of Rhode Island, 215 South Ferry Road, Narragansett, RI 02882, USA

(Received 14 June 2013; revised 19 November 2013; accepted 3 December 2013; first published online 10 January 2014)

The problem of oceanic gap-traversing boundary currents, such as the Kuroshio current crossing the Luzon Strait or the Gulf Stream traversing the mouth of the Gulf of Mexico, is considered. Systems such as these are known to admit two dominant states: leaping across the gap or penetrating into the gap forming a loop current. Which state the system will assume and when transitions between states will occur are open problems. Sheremet (*J. Phys. Oceanogr.*, vol. 31, 2001, pp. 1247–1259) proposed, based on idealized barotropic numerical results, that variation in the current's inertia is responsible for these transitions and that the system admits multiple states. Generalized versions of these results have been confirmed by barotropic rotating-table experiments (Sheremet & Kuehl, *J. Phys. Oceanogr.*, vol. 37, 2007, 1488–1495; Kuehl & Sheremet, *J. Mar. Res.*, vol. 67, 2009, pp. 25–42). However, the typical structure of oceanic boundary currents, such as the Gulf Stream or Kuroshio, consists of an upper-layer intensified flow riding atop a weakly circulating lower layer. To more accurately address this oceanic situation, the present work extends the above findings by considering two-layer rotating table experiments. The flow is driven by pumping water through sponges and vertical seals, creating a Sverdrup interior circulation in the upper layer which impinges on a ridge where a boundary current is formed. The β effect is incorporated in both layers by a sloping rigid lid as well as a sloping bottom and the flow is visualized with the particle image velocimetry method. The experimental set-up is found to produce boundary currents consistent with theory. The existence of multiple states and hysteresis, characterized by a cusp topology of solutions, is found to be robust to stratification and various properties of the two-layer system are explored.

Key words: geophysical and geological flows, quasi-geostrophic flows, stratified flows

1. Introduction

Laboratory experiments are an important tool for oceanographers who wish to explore simplified versions of more complex geophysical fluid dynamic interactions. Key elements of geophysical flow such as vertical rigidity and vorticity constraints may be modelled on rotating platforms. The rotation of the platform simulates

† Present address: Geochemical and Environmental Research Group, Texas A&M University, 833 Graham Road, College Station, TX 77845, USA. Email address for correspondence: kuehl.joe@geos.tamu.edu

https://doi.org/10.1017/jfm.2013.645 Published online by Cambridge University Press

the Earth's rotation, meridional variations of which (from the rotation vector's projection onto a spherical Earth) can be simulated in the laboratory by topographic variations. Specifically, the planetary β effect on Earth may be represented in the lab as a topographic β effect. Due to the rapid rotation of the experimental platform, the equations of motion (shallow-water equations (SWEs)) which describe the experimental flow are the same as those assumed to describe the first-order behaviour of major oceanic features (such as western boundary currents). To this end, Sheremet & Kuehl (2007) and Kuehl & Sheremet (2009) have considered rotating-table experiments of gap-traversing boundary currents. These experiments were motivated by the numerical results of Sheremet (2001), in which a barotropic boundary current with prescribed Munk profile, encountering a gap in its supporting boundary, exhibited multiple states and hysteresis. The competition between vorticity constraints (β effect) and the current's inertia is responsible for this behaviour. The simplified geometry of the system permitted experimental analysis, which confirmed a generalized version of those results (Sheremet & Kuehl 2007). An extension of those experiments further confirmed the existence of a cusp catastrophe geometry of solutions in the two-parameter space of the current's inertia and vorticity constraint magnitude (Kuehl & Sheremet 2009), two active parameters in the ocean. These results, while interesting in and of themselves, only suggest application to relevant oceanic problems.

The Luzon Strait, between Luzon Island and Taiwan, which separates the South China Sea from the Pacific Ocean, provides one area of application. The Kuroshio current forms to the south and flows north across the Luzon Strait. In the Strait region, the current assumes one of several different paths which are summarized by Caruso, Gawarkiewicz & Beardsley (2006) and more recently by Nan *et al.* (2011*a*). Another area of application is the Gulf of Maine. As Scotian Shelf water flows south, down the Scotian Shelf onto Browns bank, it encounters the Northeast Channel of the Gulf of Maine. The current has been observed either to leap the channel or to turn the corner flowing into and around the Gulf of Maine (Cho, Beardsley & Sheremet 2002). Yet another important area of application is the Gulf of Mexico loop current. The list goes on, but these locations alone provided sufficient motivation for the above studies. In an effort to improve the applicability of the experimental results to relevant oceanic problems, the present work extends the investigation of Kuehl & Sheremet (2009) in three ways. First, a new tank geometry is considered which contains a larger western basin. This allows for an eddy-shedding state which was suppressed by the former geometry. Second, the effects of stratification are investigated by considering a baroclinic (two-layer) flow. Finally, both northward- and southward-flowing currents are considered. These three additional considerations provide convincing evidence for the application of the cusp catastrophe framework to oceanic gap-traversing boundary currents.

2. Experimental set-up

The present experimental set-up is designed to mimic the generic oceanic situation in which a predominantly inertial boundary current, such as the Kuroshio (Stommel & Yoshida 1972) or Gulf Stream (Stommel 1965), encounters a gap in its supporting boundary. Observations indicate the common oceanic situation consists of a surface intensified upper layer, riding atop a weakly circulating lower layer. With this in mind, the new set-up consists of a square tank geometry depicted in figure 1, which sits atop a rotating table (rotation rate Ω is positive counterclockwise). The square tank of size

https://doi.org/10.1017/jfm.2013.645 Published online by Cambridge University Press

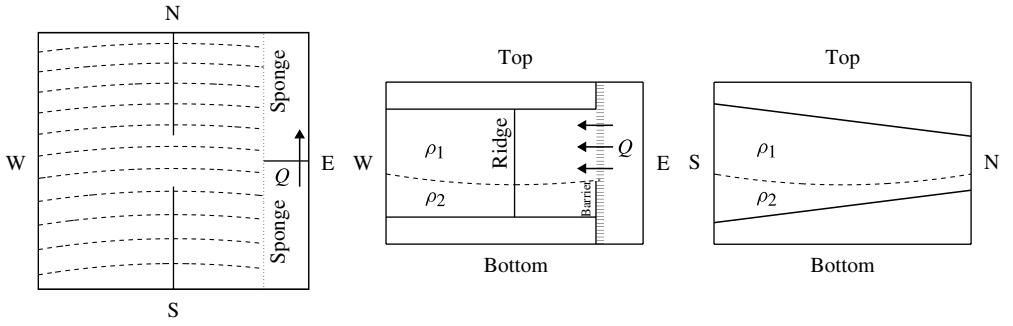


FIGURE 1. Top and side views of experimental set-up. Dashed lines in the top view indicate solid-body rotation upper-layer depth contours. Dashed line in side views indicate solid-body rotation layer interface.

$L = 76.3$ cm is partitioned into a 12 cm wide forcing region, located at the eastern side, separated from the active region by sponge barriers. North, south, east and west as referred to the laboratory set-up are introduced in analogy to the oceanic situation. The forcing region is further divided into north and south basins. In the active region, a topographic β effect is induced in the upper and lower layers by means of rigid top and bottom boundaries having opposite slope of magnitude $S = 0.1$. At the centre of the tank the boundaries are separated by $H_T = 20$ cm. A north–south running vertical ridge, which reaches from the sloping bottom to the rigid lid, divides the active region into a 37 cm wide western basin and a 27.3 cm wide eastern basin. The ridge is 1 cm thick with rounded edges and contains a gap of width $L_g = 2a = 11$ cm at its centre. For experiments with two layers of different density, in solid-body rotation, the thickness of each layer is given by

$$H_1 = H_{10} - Sy - \frac{1}{2}\frac{\Omega^2}{g}r^2 \tag{2.1a}$$

$$H_2 = H_{20} - Sy + \frac{1}{2}\frac{\Omega^2}{g}r^2, \tag{2.1b}$$

where g is the acceleration due to gravity and r is the horizontal distance from the axis of rotation, also from the centre of the tank. The resulting geostrophic contours ($2\Omega/H_1 = \text{const}$) for the upper layer (in the two-layer case), in solid-body rotation, are indicated by dashed lines in figure 1. To generate flow only in the upper layer, a rigid barrier, consistent with the parabolic shape of the interface (2.1), was inserted at $x = 27.3$ cm on the western side of the sponge, thus blocking the pumping into the lower layer. Note that only one parabolic profile was constructed ($\Omega = 1$), as it was determined to be sufficient for all experiments. This allowed for direct forcing of the upper layer, leaving the lower layer forced only through interaction with the upper layer. The upper-layer depth ($H_{10} \approx 15$ cm at the centre) is three times that of the lower layer ($H_{20} \approx 5$ cm at the centre), which results in increased relative damping of the lower layer (described below), and causes the flow to be concentrated in the upper layer similar to oceanic observations. Southward (northward) flowing boundary currents were driven by pumping fluid from the southern (northern) forcing basin to the northern (southern) forcing basin with flow rate Q (in the upper layer). This creates a pressure difference which causes fluid to percolate through the sponge boundary,

https://doi.org/10.1017/jfm.2013.645 Published online by Cambridge University Press

forming a broad Sverdrup interior flow. This interior flows west, following geostrophic contours, until impinging on the ridge, where a boundary current is formed. The boundary current must then negotiate the gap before flowing south (north) and being sucked through the southern (northern) sponge. Note that the orientation of north, south, east and west in figure 1 is consistent in all following figures.

3. Procedure

The procedure for one experiment was as follows. Warm water was stored in open containers and allowed to equilibrate with room temperature (≈20 °C). Warm water contains less dissolved gases, which reduced the formation of bubbles on the rigid lid. For the barotropic experiments, the tank was simply filled before the table was spun up. The baroclinic experiments required a special technique. Two containers of water were prepared with the same fresh water. Salt was mixed into one container before they equilibrated with room temperature. The fresh upper layer was filled first while the table was at rest. The table was then spun up, allowed to reach solid-body rotation, and the density of the fresh water was recorded. During this time, the salt water was gently stirred to remix any salt that had settled, and its density was recorded. Then the lower layer was slowly filled from the bottom of the tank with the denser salty water while the table was rotating. The lower layer was filled until the interface between layers reached the top of the parabolic insert which separated the lower-layer from the forcing region (above), at which point the tank was completely filled with fluid between the sloping bottom and rigid lid. The typical density difference between layers, $\Delta\rho = 7.5 \times 10^{-3}$ g cm^{-3}, provided a robust interface. Once filled, the tank was allowed to reach solid-body rotation. Forcing was initiated by pumping water from one forcing basin to the other at a low rate. Transient behaviour was allowed to die out, the flow was imaged with particle image velocimetry (PIV), and then the pumping rate was increased slightly. This procedure was repeated until the flow transitioned from a penetrating state to a purely leaping state, at which point the procedure was reversed with the pumping rate being slightly decreased in each step until the flow transitioned back to a penetrating state. This constituted one experiment. Several experiments were run at different table rotation rates. Between each experiment, the interface was visually checked. If the interface was not sharp and well defined, the tank was refilled.

Dye visualization was used in some experiments, but PIV was the preferred observation technique. Our PIV system works as follows. A (50 mJ) Nd-YAG laser emits a (5 ns) pulse of light through a diverging lens which converts the pulse into a horizontal sheet of light illuminating passive seed particles (glass spheres 10 μm diameter) in the fluid. The reflections are imaged by a 1376 × 1040 pixel CCD camera. The laser and camera are synchronized such that each laser pulse corresponds to one image and the time difference (90 000 μs) between two consecutive pulses (images) is known. Our system has a maximum frequency of 4 Hz. That is, four two-image pairs may be obtained every second. These settings are adequate for current velocities of a few cm s^{-1}. Once the images are recorded, software correlates the reflection patterns between two consecutive images, splitting them into smaller interrogation windows (32 × 32 pixels) which yields a two-dimensional array of velocity vectors. The laser and camera were attached to a superstructure, which was mounted around the tank, on the rotating table. The laser was mounted to the west of the tank and illuminated the gap in a horizontal plane, vertically set in the centre of the layer of interest. The camera was suspended directly above the gap. This PIV set-up allowed

https://doi.org/10.1017/jfm.2013.645 Published online by Cambridge University Press

for visualization of only one layer at a time. Thus, for the two-layer experiments, the upper and lower layers were not visualized during the same experiment.

4. Problem formulation

Though the aspect ratio of the tank is not small, the rapid rotation of the experimental platform, via the Taylor Proudman Theorem and the smallness of the Rossby number ($Ro = U/(2\Omega L)$), imparts a vertical rigidity to the fluid, making the flow predominantly two-dimensional. Thus, the SWEs may be applied to describe the flow in each fluid layer, outside of the top, bottom and interfacial viscous layers:

$$u_t - (f+\omega)v = -(p+e)_x + \nu\nabla^2 u \tag{4.1}$$

$$v_t + (f+\omega)u = -(p+e)_y + \nu\nabla^2 v \tag{4.2}$$

$$h_t + (hu)_x + (hv)_y + \mathrm{div}(\boldsymbol{\Pi}_E) = 0, \tag{4.3}$$

where u and v represent the depth-independent horizontal velocities (in the x and y directions, respectively). The total layer thickness: $h_1 = H_1 + \eta$; $h_2 = H_2 - \eta$, where H are referenced to (2.1) and η is the interface displacement downward. The effect of the viscous layers is accounted for by an Ekman flux ($\boldsymbol{\Pi}_E$). The Ekman layer depth, $h_E = \sqrt{\nu/\Omega} \approx 0.1$ cm, is small compared with the layer depth, p is the pressure anomaly relative to solid-body rotation divided by water density (ρ), $e = (u^2 + v^2)/2$ is the kinetic energy, ν is the viscosity and $f = 2\Omega$ is the Coriolis parameter.

The dynamical equations for the potential vorticity, $q = (f+\omega)/h$, where $\omega = v_x - u_y$ is the relative vorticity, in the vorticity–stream function formulation are obtained in the traditional way by taking curl of the momentum equations (4.1) and (4.2) and substituting the flow divergence from the layer thickness (4.3). In doing so it is convenient to decompose the flow into non-divergent and divergent layer transport components $h\boldsymbol{u} = \hat{k} \times \boldsymbol{\nabla}\psi + \boldsymbol{\nabla}\varphi$:

$$\omega_{1t} + J(\psi_1, q_1) - q_1\eta_t = -q_1\frac{h_E}{2}\left(\omega_1 + \frac{\gamma}{2}\Delta\omega\right) + \nu\nabla^2\omega_1 \tag{4.4a}$$

$$\omega_{2t} + J(\psi_2, q_2) + q_2\eta_t = -q_2\frac{h_E}{2}\left(\omega_2 - \frac{\gamma}{2}\Delta\omega\right) + \nu\nabla^2\omega_2, \tag{4.4b}$$

where $\Delta\omega = \omega_1 - \omega_2$, and subscripts 1 and 2 correspond to the upper and lower layers, respectively. The divergent component caused by the Ekman suction is small ($\varphi/\psi \approx h_E/h = O(10^{-2})$) so φ can be neglected in the vorticity advection terms. Also, φ can be neglected in the elliptic equation relating vorticity and stream function (following directly from the above decomposition)

$$\boldsymbol{\nabla}\left(\frac{1}{h}\boldsymbol{\nabla}\psi\right) + J\left(\frac{1}{h}, \varphi\right) = \omega. \tag{4.5}$$

To the first order in Rossby number, the approximation for the divergence of the Ekman flux is represented by terms $(h_E/2)\omega$ (at solid boundaries) and $\pm(\gamma h_E/4)\Delta\omega$ (at the fluid layer interface). The factor γ, $0 \leqslant \gamma \leqslant 1$, represents the reduced efficiency of the Ekman suction at a fluid interface of finite density thickness (existing in the laboratory experiment) compared with the idealized case of an infinitely thin density interface.

The hydrostatic approximation, valid for slow motion, is used to relate the pressure difference in the two layers with the downward interface displacement

$$p_1 - p_2 = g'\eta. \tag{4.6}$$

https://doi.org/10.1017/jfm.2013.645 Published online by Cambridge University Press

Combining this with the dominant geostrophic balance between the Coriolis term and the pressure gradient in (4.1) and (4.2) results in the equation for the interface displacement

$$g'\nabla^2\eta = f(\omega_1 - \omega_2) \tag{4.7}$$

with appropriate boundary conditions following from (4.1) and (4.2). Total layer mass conservation must also be specified as a solvability condition for the Neuman problem.

Note in ((4.4)) (via ((4.5))) the frictional divergence term is inversely proportional to layer depth. The regular lateral and Ekman bottom friction are comparable in the western boundary current region in these experiments as characterized by the non-dimensional coefficients defined in Sheremet & Kuehl (2007). By choosing an upper-layer depth approximately three times greater than the lower-layer depth, the lower layer is damped with an exponential decay rate three times greater than the upper. As friction is unavoidable in the lab, it has been taken advantage of to create a situation which mimics the ocean by preferential damping of the lower layer, resulting in an upper-layer intensified flow. Typical upper-layer velocity was found to be between 1 and 0.1 cm s^{-1}, while lower-layer flows rarely exceeded 0.01 cm s^{-1}.

Geophysical boundary currents are typically characterized by balancing bottom drag, vertical friction or advective terms against the β effect to give Stommel, Munk and inertial boundary layers, respectively. However, in the present case interest lies in the gap region where several dominant balances are worth note. In the following, $Ro = \omega/f \ll 1$, $h_E/H \ll 1$ and $\eta \ll H$ have been assumed. Application of the geostrophic assumption at leading order follows from quasi-geostrophic and quasi-hydrostatic balances, coupled with near-zero lower-layer flow (both observed and expected due to lack of direct forcing and enhanced vorticity decay). In addition, it is standard to expand the advective term ($J(\psi, q)$) to show the topographic beta effect ($\beta = H\partial q/\partial y$ or on average fS/H).

From this point on the subscripts (1, 2) will be dropped, it will be assumed that all variables are referenced to the upper layer and the flow in the lower layer is negligible. The low-inertia, steady-flow case results in the so-called β-plume solution (Gill & Smith 1970; Stommel 1982) consisting of a weak zonal flow in which lateral dispersion balances the β effect

$$\beta\psi_x = -\frac{fh_E}{2H}\left(1 + \frac{\gamma}{2}\right)\psi_{yy} + \nu\psi_{yyyy}. \tag{4.8}$$

The other low-inertia balance of note describes the decay of geostrophic current by Ekman pumping. Generally speaking, the vorticity evolution in both layers is coupled due to the interfacial displacement. However, for horizontal scales much smaller than the Rossby radius of deformation, that coupling becomes small and the equation reduces to

$$\omega_t = -\frac{fh_E}{2H}\left(1 + \frac{\gamma}{2}\right)\omega, \tag{4.9}$$

which leads to an Ekman decay time scale, $T_e = H/(h_e\Omega(1 + \gamma/2))$. The above two balances describe the gap-penetrating flow states in which inertia is sufficiently weak and the boundary current turns into the gap region forming a primarily zonal flow.

In contrast, the high inertia case consists of a gap-leaping flow in which advection is balanced by the β effect. Consider the simplified version of (4.4), written for a single

https://doi.org/10.1017/jfm.2013.645 Published online by Cambridge University Press

fluid layer

$$\beta\psi_x + J(\psi, \omega) - \frac{f}{H}J(\psi, \eta) = -\frac{fh_E}{2}\left(1 + \frac{\gamma}{2}\right)\omega + \nu H\nabla^2\omega, \tag{4.10}$$

which, when the right-hand side is small, states that potential vorticity is approximately conserved along a streamline. Typical values of variables in the gap region are substituted in order to compare terms in (4.10) (i.e. spatial dimensions are a, $\beta = 2S\Omega/H$, $\eta \approx f(\psi - \psi_0(y))/(g'H)$, $\omega \approx Q/(Ha^2)$ and $L_R = \sqrt{g'H}/f$), and the equation is non-dimensionalized by bottom friction (multiply by a^2T_e/ψ). The following non-dimensional coefficients result:

$$\frac{\beta \text{ term}}{\text{bottom friction}} \rightarrow K_V = \frac{2aS}{h_E(1 + \gamma/2)} \approx \mathcal{O}(10) \tag{4.11}$$

$$\frac{\text{advection term}}{\text{bottom friction}} \rightarrow K_I = \frac{Q}{a^2h_E\Omega(1 + \gamma/2)} \approx \mathcal{O}(10) \tag{4.12}$$

$$\frac{\text{interfacial term}}{\text{bottom friction}} \rightarrow K_S = \frac{\psi - \psi_0}{L_R^2h_E\Omega(1 + \gamma/2)} \approx \mathcal{O}(1) \tag{4.13}$$

$$\frac{\text{lateral friction}}{\text{bottom friction}} \rightarrow K_F = \frac{\nu H}{a^2h_E\Omega(1 + \gamma/2)} < \mathcal{O}(0.1). \tag{4.14}$$

Substitution of typical values suggests, as expected, that the dominant balance for the gap-leaping flow will be between advection and the β effect. The terms in (4.10) may be understood by considering the gap as a topographic potential vorticity barrier (βa) which the boundary current must overcome to leap across. If the inertia of the current is insufficient, the flow will follow geostrophic contours in a gap-penetrating state. Here K_I is a measure of the inertia working to overcome the topographic potential vorticity barrier, K_V can be interpreted as the topographic potential vorticity barrier provided by the gap, which must be traversed faster than T_e, to justify neglect of the viscous terms, K_S is a small correction term describing the influence of a deformable layer interface, and the small value of K_F illustrates the dominance of bottom friction over lateral friction in the gap region.

In order to completely solve the problem, an equation for η is needed. Following Charney (1955), it is assumed that outside the western boundary layer the Bernoulli function and potential vorticity are conserved and there is a functional relationship between η and ψ. This relationship is set at the sponge boundary and leads to the approximate relationship $\eta = f(\psi - \psi_0(y))/(g'h)$. In the western boundary layers, a semigeostrophic balance (a geostrophic balance only across the flow) $\eta_x = f\psi_x/(g'h)$ is applied, which will allow for calculation of an approximate two-layer boundary current structure.

5. Experimental results

5.1. *Baroclinic*

Figure 2 shows the results of a typical experiment. Beginning with low transport, the boundary current does not have sufficient inertia to overcome the topographic potential vorticity barrier required to leap the gap. Instead, the current turns into the gap following geostrophic contours in a gap-penetrating β-plume-type solution. As the transport of the boundary current is increased, the gap-penetrating flow state persists, but now the current has sufficient inertia to cross some geostrophic contours. The

https://doi.org/10.1017/jfm.2013.645 Published online by Cambridge University Press

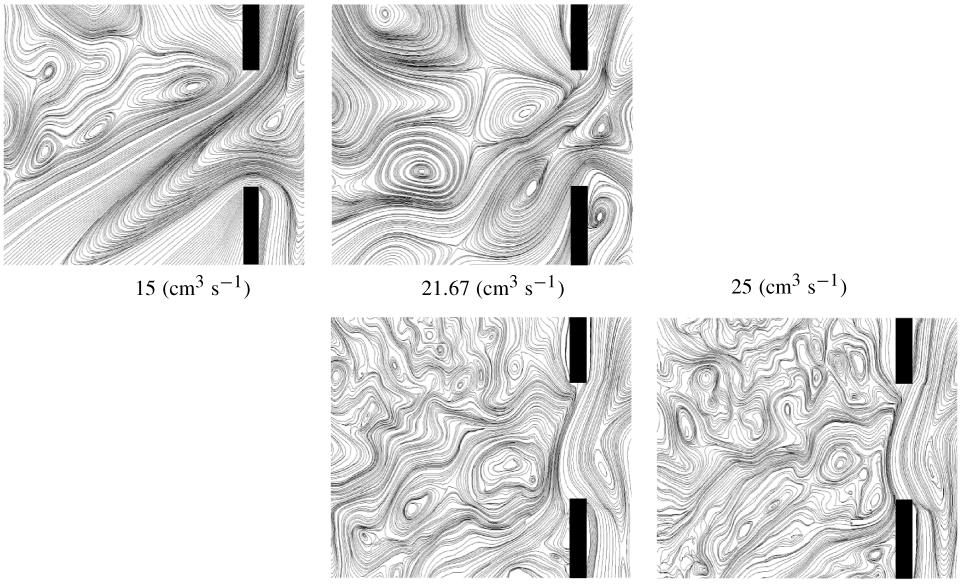


FIGURE 2. Baroclinic flow patterns illustrating hysteresis in the upper-layer as the strength of the current (cm^3 s^{-1}) is varied ($\Omega = 1.0$ rad s^{-1}). Upper figures illustrate increasing flow strength, while lower figures illustrate decreasing flow strength. Thick black lines mask the ridge. Shown are 'flow lines' which are everywhere tangent to the velocity. Note, unlike streamlines, line density does not related to flow strength and thus patterns in both weak and strong flow regions are clearly visible.

flow in this case forms a loop current, which may be steady or may shed eddies to the west. As the transport of the boundary current is increased further, its inertia becomes sufficient to overcome the topographic potential vorticity barrier in the gap and the current is able to leap across the gap with minimal penetration. The transition from a gap-penetrating flow state to a gap-leaping flow state is abrupt. Once in the gap-leaping flow state, the transport of the current may be reduced and the gap-leaping flow state will persist. Not until the transport is reduced to a sufficiently low level does the system abruptly transition back to the gap-penetrating flow state.

At a particular table rotation rate (Ω) and gap width ($2a$), the system is seen to exhibit hysteresis as the transport (Q) of the current is varied. Experiments were run to span the K_V, K_I parameter space and it is found that the width of the hysteresis region is dependent on K_V. As described in Kuehl & Sheremet (2009), the state of the system may be identified by the western extent of the current in the gap region (X_P) and that when considering the dependence of the state of the system on K_V and K_I, the system is found to display a cusp catastrophe geometry of solution. It is convenient to consider the bifurcation set of the catastrophe surface by projection onto the parameter space (figure 3). The bifurcation set identifies the critical parameters at which the system transitions between leaping and penetrating flow states. Between the branches of the bifurcation set (Region 3) the system admits multiple flow states. Region 1 is characterized by a steady gap-leaping flow state (figure 2 lower). Region 2 is characterized by a penetrating flow state which consists of a steady or eddy-shedding loop current (figure 2 upper). Region 3 is the region of multiple states. Which flow state the system assumes in Region 3 depends upon how Region 3 is approached. If

https://doi.org/10.1017/jfm.2013.645 Published online by Cambridge University Press

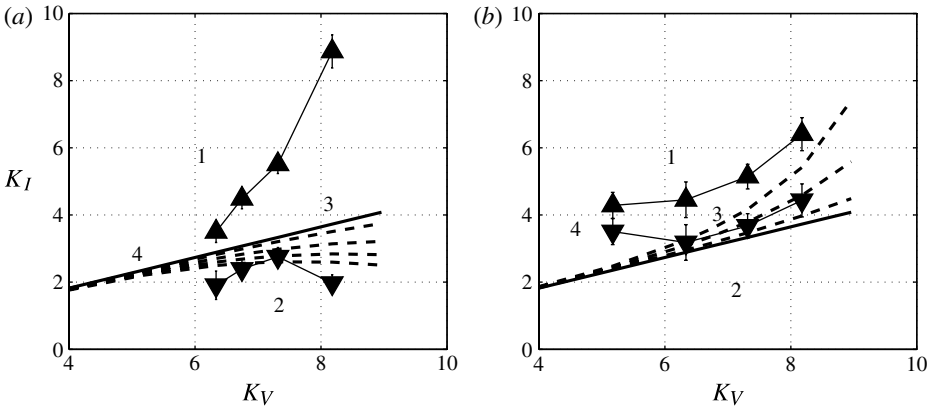


FIGURE 3. Bifurcation set for baroclinic experiments: (*a*) northward-flowing boundary current (*b*) southward-flowing boundary current. Region 1 indicates leaping states, Region 2 indicates penetrating states, Region 3 is the region of multiple states and Region 4 indicates where hysteresis is no longer present. Symbols indicate experimental data, solid lines are theoretical predictions from (6.4) without interface displacement effects and dashed lines represent 10, 30, 50 and 70 % interface rebound. Error bars indicate the flow rate step size during an experiment.

it is approached from a penetrating flow state (Region 2), it will continue to penetrate until the upper branch of the bifurcation set is reached. This upper branch represents the transitions from penetrating to leaping. If Region 3 is approached from a leaping flow state (Region 1), the system will remain in the leaping state until the lower branch of the bifurcation set is crossed. This lower branch represents the transitions from leaping to penetrating. In Region 4, multiple states are no longer present and the state of the system transitions smoothly between leaping and penetrating. The upper and lower branch curves coalesce in Region 4; however, the authors did not have the possibility to experimentally pinpoint where this happens precisely in the parameter space. Again, a more thorough explanation of the cusp catastrophe behaviour may be found in Kuehl & Sheremet (2009).

The new experimental design admits an eddy-shedding loop current state. In the former geometry (Sheremet & Kuehl 2007; Kuehl & Sheremet 2009), the gap-to-outer-wall distance was approximately the same as the gap width. As the gap width sets the length scale of the loop current (and shed eddies), the eddy-shedding state was suppressed through viscous interactions with the outer tank wall. With this restriction removed, the flow transitions from a steady loop current state, (figure 4 filled circles) at low flow rates, to an eddy-shedding loop current (figure 4 open circles) as the flow rate increases. The eddy-shedding state continually spins up and sheds eddies form the centre of the loop current with a period that depends on both platform rotation rate and flow rate (figure 5). The trend of increasing period with increasing flow rate and decreasing period with increasing rotation rate observed in the barotropic case (described below) appear to hold for the baroclinic case. For instance, at $\Omega = 1.25$ rad s^{-1} the period increases ($T_{eddy} = 175, 200, 235$ s) for increasing flow rate ($Q = 20, 25, 30$ cm^3 s^{-1}, respectively). Also at $Q = 20$ cm^3 s^{-1} the period decreases ($T_{eddy} = 215, 175$ s) for increasing rotation rate ($\Omega = 1.0, 1.25$ s^{-1}).

https://doi.org/10.1017/jfm.2013.645 Published online by Cambridge University Press

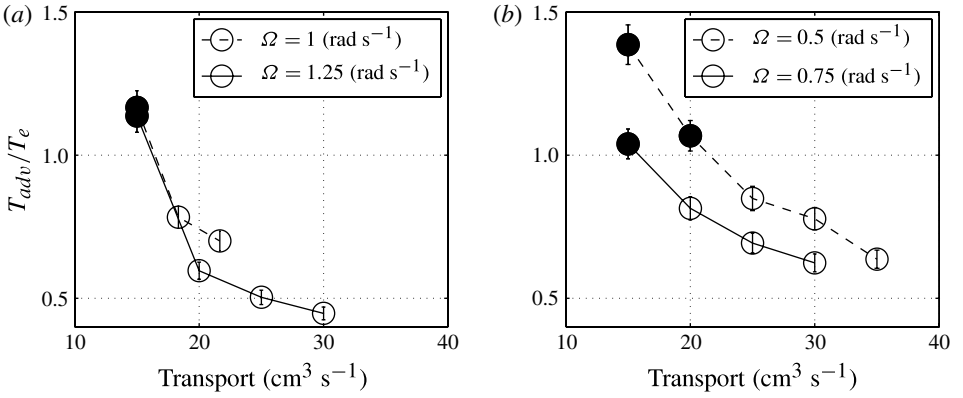


FIGURE 4. (*a*) Baroclinic and (*b*) barotropic non-dimensional advective time for steady (filled symbols) and eddy-shedding (open symbols) loop current states against transport (Q) for different rotation rates (Ω). Here $\gamma = 0.5$ is shown for the baroclinic case. Error bars represent 10 % uncertainty in the measurement velocity as described in the text.

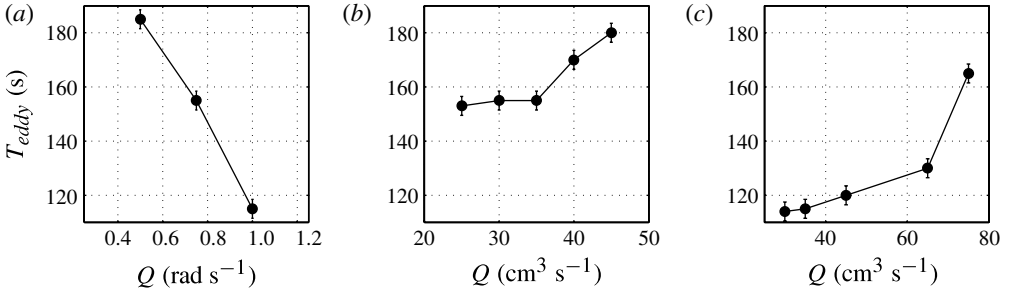


FIGURE 5. Barotropic eddy-shedding period plotted against rotation rate (Ω) and flow rate (Q): (*a*) $Q = 35$ (cm^3 s^{-1}); (*b*) $\Omega = 0.75$ (rad s^{-1}); (*c*) $\Omega = 1$ (rad s^{-1}). The T_{eddy} calculations were found to be periodic within 7 s as described in the text.

5.1.1. *Baroclinic boundary current structure*

Additional experiments were run ($\Omega = 1$ rad s^{-1}) to investigate the structure of the boundary current in the two-layer case (figure 6). Only the upper layer was visualized, and it is assumed the lower-layer flow is very weak. Note the difference between northward- and southward-flowing currents. As the transport of the current increases, the northward-flowing current tends to broaden (wider current with small peak velocity increase), whereas the southward-flowing current tends to intensify (increases peak velocity with less broadening). As expected, the presence of a deformable interface has broken the north–south invariance of the system.

5.2. *Barotropic*

The dynamics of barotropic gap-leaping boundary currents have been treated by Sheremet (2001), Sheremet & Kuehl (2007) and Kuehl & Sheremet (2009). However, to investigate the dynamics of the eddy-shedding loop current state more thoroughly, barotropic experiments were conducted. As described above, the eddy-shedding state continually spins up and sheds eddies from the centre of the loop current with a period

https://doi.org/10.1017/jfm.2013.645 Published online by Cambridge University Press

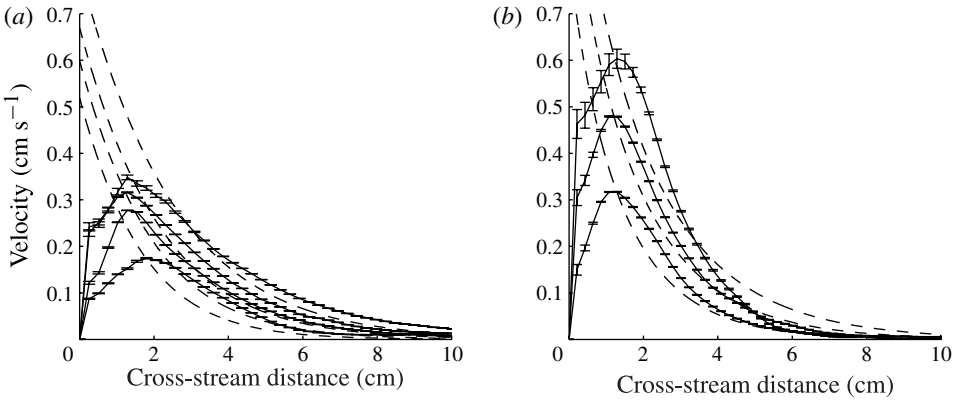


FIGURE 6. Comparison of experimental (solid) and numerical (dashed, Charney formulation) boundary current velocity profiles: (*a*) northward; (*b*) southward. The rotation rate is $\Omega = 1$ rad s^{-1} and northward pumping rates are $Q = 15, 20, 25, 35$ cm^3 s^{-1} while southward pumping rates are $Q = 20, 30, 40$ cm^3 s^{-1}. Error bars indicate standard error.

that depends on both platform rotation rate and flow rate (figure 5). Note that the period decreases with increasing rotation rate and increases with increasing flow rate. The eddy-shedding period's dependence on flow rate appears to have two stages: one in which the period slowly increases and another with rapid increase. As an additional note, the north–south invariance of the barotropic case was confirmed for the current tank geometry.

6. Discussion

6.1. *Boundary current structure*

An important result of the baroclinic experiments is the north–south asymmetry displayed in the boundary current structure and bifurcation set. To understand this deviation from north–south invariant quasi-geostrophic dynamics, consider the formulation of Charney (1955) in which potential vorticity and Bernoulli function are conserved along streamlines (transport lines) to obtain an outer boundary current structure (neglecting the viscous sublayer).

The experimental set-up admits a constant inflow (U_0) at the sponge barrier. Assuming this weak inflow is geostrophic, we are able to obtain the ideal interface displacement (η_0) relative to solid-body rotation along the barrier. This, along with the known upper-layer depth due to the rigid lid at the barrier (H_0), can be integrated to yield transport along the barrier: $\psi_{02} - \psi_{01} = U_0 \int_{y_1}^{y_2} (H_0 + \eta_0)\, \mathrm{d}y$. Thus, the Bernoulli function and potential vorticity, both of which can be expressed as a function of ψ only, may be specified along the barrier. With boundary conditions now known at the barrier, Charney's formulation may be used to solve for the boundary current structure (figure 6). The numerics show reasonable agreement with the experimental data. However, it must be remembered that Charney's formulation neglects viscosity, assumes no lower-layer flow, assumes a perfectly uniform inflow and assumes purely east–west interior geostrophic flow. Friction is obviously present in the experiment along with a small (but non-zero) lower-layer flow. Also, the inflow along the sponge is not perfectly uniform (particularly at the edges) and the interior flow is not purely east–west. Figure 1 shows that the geostrophic contours in solid-body rotation bend

https://doi.org/10.1017/jfm.2013.645 Published online by Cambridge University Press

slightly northward. For southward flow, the geostrophic contours intersect the northern wall and create a boundary current. This current is expected to be weak due to the reduced inflow near the edges of the sponge as well as the small curvature of the geostrophic contours.

Focusing back on the experimental data (figure 6), when northward- and southward-flowing currents are compared, note that the southward-flowing currents are narrower and more intense than the broader weaker northward-flowing currents. Given above are several experimental set-up reasons for deviation from standard theory, however a key observation is to consider the trends in the velocity profiles as flow rate increases. For northward-flowing currents, observe the typical behaviour with a growing exponential tail, much like an inertial boundary current. For southward-flowing currents, the boundary current displays a fixed width. As transport is increased, the magnitude of the current increases, but the spatial extent remains fairly constant. This effect is likely due to the deviation from quasi-geostrophic dynamics allowed by a deformable interface (assuming weak current formation on the northern wall). Consider the relation between velocity and transport function $v = \psi_x/h$. Expansion about the small interface displacement $v = (\psi_x/H)(1 - \eta/H)$, with $\eta = f(\psi - \psi_0)/g'H$ consistent to leading order, yields $v = \psi_x/H - f(\psi - \psi_0)_x^2/(2g'H^3)$. The second term in the expansion is an ageostrophic term neglected by quasi-geostrophic dynamics which represents advection of the interface by the geostrophic flow and results in a southward-flow component. In the equations of motion, this term is multiplied by f, giving $fv = (\psi_x/H)(f - (f^2/g'H)(\psi - \psi_0)/H)$ and the dependence on a finite radius of deformation, $L_R^2 = g'H/f^2$, is clear. This term will affect southward-flowing currents more strongly than northward-flowing currents, due to its dependence on velocity magnitude. Northward-flowing currents are weakened and broadened by this ageostrophic term, thus lessening the effect and only a slight deviation from an inertial type boundary current structure is observed. Southward-flowing currents are amplified by this ageostrophic term, thus increasing the effect and significant deviation from an inertial type boundary current structure is observed.

6.2. *Bifurcation set branches*

The main result of this paper is the continued presence of the cusp catastrophe behaviour in time-dependent and stratified gap-traversing boundary currents flowing either northward or southward. The essence of the catastrophe theory as applied to this problem is as follows. The (averaged) state of the system depends on two non-dimensional parameters, which are chosen to be K_I and K_V, indicating the strength of flow inertia and vorticity constraints, respectively. The flow pattern can be characterized, among various possible choices, by the distance (X_P) the loop current penetrates westward through the gap. The function $X_P(K_I, K_V)$ is multivalued in certain regions of the parameter space K_I, K_V. For example, as described in § 5.1, a plot of X_P during a typical experiment would trace a hysteresis curve at specified K_V as K_I is varied in a quasi-stationary manner (or vice versa). If viewed in a three-dimensional space, the surface, $X_P(K_I, K_V)$, represents two folds coalescing at a cusp point (Thom 1972, 1975; Arnold 2004). That is, the width of the hysteresis region in parameter space varies, and the limiting parameters for which hysteresis is no longer present demark the cusp point (where two folds coalesce). As described in Kuehl & Sheremet (2009), the dynamics of gap-leaping boundary currents may be understood by tracing the state of the system along the surface, $X_P(K_I, K_V)$, as the parameters of the system are varied. Rapid transitions between states occur when the system parameters are varied in such a way that the state of the system 'falls off'

https://doi.org/10.1017/jfm.2013.645 Published online by Cambridge University Press

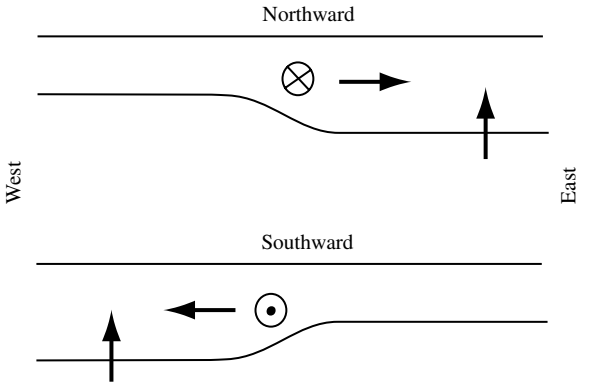


FIGURE 7. Sketch illustrating the influence of a deformable interface on the jet as it crosses the gap. Arrows indicate motion of interface and jet motion when the transport of the current is decreased.

the upper portion of the surface onto the lower portion at a fold (or vice versa). One consequence of the catastrophe theory is that the choice of two different control parameters other than K_I, K_V (which can be ultimately expressed in terms of K_I, K_V) will not change the topology of the cusp catastrophe: the folds and the cusp will remain. When projected onto the K_I, K_V plane, the folds indicate the position of the bifurcation set (figure 3) which conveniently summarizes the system's dynamics. Kuehl & Sheremet (2009) provide a simple potential vorticity conservation scheme to describe the lower branch of the barotropic bifurcation set which predicts a linear relation between the boundary current maximum velocity (V_m) and rotation rate (Ω). Figure 3 shows the deviation from this linear dependence resulting from a deformable interface. To explain this behaviour, consider a cross-section of the current in the gap region as it leaps the gap (figure 7). The straight top line indicates the rigid lid with interface displacement indicated by the curved line. The arrows indicate the trend as transport of the current is decreased. For a northward-flowing current, the eastern part of the interface will rebound (squishing the upper layer). This causes the gap-leaping jet to migrate eastward in order to conserve potential vorticity. Thus, the transition from a leaping to a penetrating flow state will be shifted towards lower flow rates, which is consistent with our observations. For a southward-flowing current, the opposite will happen. In this case, the western part of the interface will rebound (squishing the upper layer), which induces the gap-leaping jet to migrate westward. Thus, the transition from a leaping to a penetrating flow state will be shifted to higher flow rates, again consistent with our observations.

It is difficult to obtain a scaling relation for this effect. However, an attempt to generalize the transition condition of Kuehl & Sheremet (2009) to the baroclinic case is attempted by considering the interface displacement as a perturbation to the fluid depth. Returning to (4.10) and making the assumption that meridional advection is balanced by the β effect:

$$\left(\frac{\mathrm{d}V}{\mathrm{d}n} - KV\right)_y - \frac{f}{h}\eta_y + \beta = 0, \tag{6.1}$$

where relative vorticity has been expressed in terms of cross-stream shear ($\mathrm{d}V/\mathrm{d}n$), velocity magnitude V and curvature K. Upon integration, $\int_a^b () \, \mathrm{d}y$, and by choosing

https://doi.org/10.1017/jfm.2013.645 Published online by Cambridge University Press

to trace a streamline which corresponds to the maximum velocity of the current (the existence of which was explicitly shown by Sheremet and Kuehl for barotropic flow, but must be assumed in the present case), $\mathrm{d}V/\mathrm{d}n \approx 0$ and solve for K:

$$K = \frac{f\left[S\left(y_b - y_a\right) - \left(\eta_b - \eta_a\right)\right]}{HV_m}. \tag{6.2}$$

The critical transition condition: the radius of curvature ($R_c = K^{-1}$), evaluated in the middle of the gap ($y_b - y_a = a$) and thus the radius of the newly formed eddy, will be equal to the half-width of the gap, a. Solve for V_m, to obtain

$$V_m = \frac{fR_c}{H}\left[Sa - \left(\eta_b - \eta_a\right)\right] = \frac{fSa^2}{H} - \frac{fa\left(\eta_b - \eta_a\right)}{H}. \tag{6.3}$$

Note that for a northward-flowing current $(\eta_b - \eta_a) > 0$ while for a southward-flowing current $(\eta_b - \eta_a) < 0$, remembering the definition of η. The important point to note is the influence of the interfacial displacement relative to the barotropic case ($V_m = (fSa^2)/H$). For northward-flowing currents V_m is reduced, making it more difficult to transition from a gap-leaping flow state to a gap-penetrating flow state. While for a southward-flowing current, V_m is increased making it easier to transition. This result is consistent with both the explanation given in the beginning of this section as well as the experimental observations (figure 3).

To quantify the influence of this effect more precisely, the interface rebound $(\eta_b - \eta_a)$ must be known. This may be estimated by applying Charney's formulations and roughly relating maximum velocity to transport as $Q = V_m(\delta H)/2$, where δ is the approximate length of the boundary layer (L_b) or viscous sublayer (L_ν). In addition, it is assumed that some fraction, α, of the interface rebounds. These assumptions lead to the approximate transition relationship

$$Q = \beta a^2 \frac{L_b H}{2}\left[1 \pm \frac{\alpha a L_\nu}{L_R^2}\right]^{-1}. \tag{6.4}$$

With $L_b \approx 5$ and $L_\nu \approx 2$, good agreement with the experimental data is found. Note these approximations are rough and larger L_b gives better agreement for northward-flowing currents. However, an effort was made to avoid curve fitting. This simple result strongly supports the above critical transition condition.

6.3. *Eddy-shedding state*

Another key observation in this work, is the existence of both steady and eddy-shedding gap-penetrating states. This eddy-shedding state is fundamentally different from an eddy-shedding event which can occur when the system transitions from gap leaping to gap penetrating. Thus, if one is considering observational data of eddy formation, it is important to differentiate between eddies formed during a transition event and eddies formed as part of an eddy-shedding state. Eddies formed as part of the eddy-shedding state can be understood by considering figure 4. Only the experiments for which several steady and eddy-shedding penetrating states were present are shown, but this relation holds for all experiments performed. For weaker penetrating flows, Ekman dissipation is capable of dissipating the vorticity being advected into the western basin. As the flow rate increases, Ekman dissipation can no longer balance vorticity advection and the advected vorticity is then dissipated from the current in the form of westward-travelling eddies. This mechanism for the explanation/prediction of eddy formation appears to be consistent with the 'momentum

https://doi.org/10.1017/jfm.2013.645 Published online by Cambridge University Press

imbalance paradox' of Pichevin & Nof (1997) with the addition of viscosity, though we have not yet shown a rigourous relationship. Pichevin and Nof use a convenient integration path in their calculations which the current geometry does not allow. Note that the advective time scale is based on measured experimental velocity and twice the gap length ($T_{adv} = 2L_g/V$), the barotropic case accounts for both top and bottom Ekman layers, and the baroclinic case accounts for one solid Ekman layer and one fluid interface. In the figure $\gamma = 0.5$ is shown, however the above arguments are found to be consistent with any $\gamma \geqslant 0.2$.

In addition, the eddy-shedding period is consistent with simple β drift of an isolated eddy. Assuming the eddy-shedding period to be the time taken for an eddy to drift one eddy diameter ($T = 2R_e/V_d$ with $V_d = 2SR_eV_c/h_0$), the observed eddy-shedding periods (figure 5*a*), $T = 180$, 155 and 120 s, yield circulation velocities, $V_c = 0.55, 0.65$ and 0.83 cm s^{-1}, respectively. These correspond well with boundary current maximum velocities, $V_c = 0.55$, 0.65 and 0.74 cm s^{-1}, calculated with an idealized one-dimensional boundary-layer model (shown to work well in Kuehl & Sheremet (2009)). The slight increase in T with flow rate (figure 5*b,c*) appears to be due to the momentum of the current pushing the eddies further south, into deeper water, thus decreasing β. While the rapid increase in period appears to be related to the current's interaction with the southern gap edge. This increase in friction acts to dissipate more energy, and leads to a longer eddy formation time.

The eddy-shedding period was measured in two ways. (i) By recording 3–5 eddy-shedding periods of PIV velocity fields taken at 1 Hz. This required large data storage and long computational processing times. (ii) More commonly, by timing eddy-shedding periods in realtime. Typically, 5–10 eddy-shedding periods were measured. The main uncertainty in either case was identification of a particular phase in the eddy-shedding process on which to base these times. Method 1 identified periods to within four frames (total uncertainty of 4 s), but was used sparingly. Method 2 was less accurate, but found no variation larger than 7 s (total uncertainty). This 'worst case' estimate is applied as the error bars in figure 5. Concerning PIV velocity measurements (figures 4 and 6), the largest factors affecting velocity uncertainty are due to non-uniform particle seeding, reflections near the boundary edge and laser shadows from the experimental set. Shown in figure 6 are standard error bars of the boundary current velocity profile. Consistent with figure 6, uncertainty in the velocity measurements used to calculate the advective time scale (T_{adv}) are found to be no greater than 10 % and often smaller. Again, this 'worst case' estimate is applied in figure 4 to illustrate the robustness of the measurements.

It is interesting to contrast the dynamics of the eddy-shedding state observed in these experiments with observations of loop current frontal eddies (Fratantoni *et al.* 1998; Oey 2008). In the case of the Gulf of Mexico, it would appear that the excess vorticity spins up loop current frontal eddies as a mechanism to dissipate vorticity. These eddies may then suppress the periodic eddy-shedding state by maintaining a steady vorticity balance and/or cause eddy-shedding events by cleaving the loop current.

7. Conclusion

Laboratory experiments of two-layer, gap-traversing, predominantly inertial boundary currents have been presented. The experimental observations agree well with predictions based on the SWEs and quasi-geostrophic dynamics. The key feature observed was the continued presence of multiple states, which appear to be described

https://doi.org/10.1017/jfm.2013.645 Published online by Cambridge University Press

by the cusp catastrophe framework. In addition, the system was found to admit three distinct states: a steady gap-leaping state, a steady gap-penetrating loop current state and an eddy-shedding loop current state. The transition between the latter two appears to be due to the relative strengths of vorticity advection into the gap and vorticity dissipation due to friction (predominantly Ekman friction). If friction is strong enough to balance vorticity advection, the system will assume a steady loop current state. Once vorticity advection overcomes friction, the excess vorticity is dissipated by eddy shedding. These idealized dynamical mechanisms may benefit observational efforts such as Nan *et al.* (2011*b*), who identify eddy production south of Taiwan or Lu & Liu (2013) and Sheu, Wu & Oey (2010) who have shown the leaping path of the Kuroshio to efficiently block westward propagation of eddies into the South China Sea. Finally, the two-layer boundary current structure for southward-flowing currents was found to be narrower and more intense than for northward-flowing currents. This behaviour is consistent with the layered boundary current theory of Charney, but is best understood by considering the interfacial displacement as a perturbation, leading to an ageostrophic term, which accounts for the observed behaviour.

The results of this work significantly progress the cusp framework toward application in realistic ocean conditions. Note this progress is supported by the work of Yuan & Wang (2011) who numerically studied the 1.5-layer gap-leaping problem. It was shown that eddy activity can modify the gap-leaping dynamics through influencing the boundary current, but the basic vorticity balance and cusp framework persist as the fundamental dynamics of the system.

Acknowledgements

This work was funded through NSF Grant 796475382 and in part by a grant from BP/The Gulf of Mexico Research Initiative. The authors are grateful to the Geophysical Fluid Dynamics Laboratory at the Graduate School of Oceanography, where these experiments were run and to Dr P. Cornillon for overseeing the lab and many fruitful discussion during the course of this project.

REFERENCES

ARNOLD, V. I. 2004 *Catastrophe Theory*. Springer.

CARUSO, M. J., GAWARKIEWICZ, G. G. & BEARDSLEY, R. C. 2006 Interannual variability of the Kuroshio intrusion in the South China Sea. *J. Oceanogr.* **62**, 559–575.

CHARNEY, J. G. 1955 The gulf stream as an inertial boundary layer. *Proc. Natl Acad. Sci. USA* **41**, 731–740.

CHO, Y. K., BEARDSLEY, R. C. & SHEREMET, V. A. 2002 On the cause of Scotian shelf water crossovers. *Geophys. Res. Lett.* **29**, 2212.

FRATANTONI, P. S., LEE, T. N., PODESTA, G. P. & MULLER-KARGER, F. E. 1998 The influence of loop current perturbations on the formation and evolution of tortugas eddies in the southern straits of Florida. *J. Geophys. Res.* **103**, 24759–24779.

GILL, A. E. & SMITH, R. K. 1970 On similarity solutions to the differential equation $\psi_{zzzz} + \psi_x = 0$. *Proc. Camb. Phil. Soc.* **67**, 163–171.

KUEHL, J. & SHEREMET, V. A. 2009 Identification of a cusp catastrophe in a gap-leaping western boundary current. *J. Mar. Res.* **67** (1), 25–42.

LU, J. & LIU, Q. 2013 Gap-leaping Kuroshio and blocking westward-propagating Rossby wave and eddy in the Luzon Strait. *J. Geophys. Res.* **118**, 1170–1181.

MORGAN, G. W. 1956 On the wind-driven ocean circulation. *Tellus* **8**, 301–320.

NAN, F., XUE, H., CHAI, F., SHI, L., SHI, M. & GUO, P. 2011*a* Identification of different types of Kuroshio intrusion into the South China Sea. *Ocean Dyn.* **61**, 1291–1304.

https://doi.org/10.1017/jfm.2013.645 Published online by Cambridge University Press

NAN, F., XUE, H., XIU, P., CHAI, F., SHI, M. & GUO, P. 2011*b* Oceanic eddy formation and propagation southwest of Taiwan. *J. Geophys. Res.* **116**, C12045.

OEY, L. Y. 2008 Loop current and deep eddies. *J. Phys. Oceanogr.* **38**, 1426–1449.

PICHEVIN, T. & NOF, D. 1997 The momentum imbalance paradox. *Tellus* **49A**, 298–319.

SHEREMET, V. A. 2001 Hysteresis of a western boundary current leaping across a gap. *J. Phys. Oceanogr.* **31**, 1247–1259.

SHEREMET, V. A. & KUEHL, J. 2007 Gap leaping western boundary current in a circular tank model. *J. Phys. Oceanogr.* **37**, 1488–1495.

SHEU, W.-J., WU, C.-R. & OEY, L.-Y. 2010 Blocking and westward passage of eddies in the Luzon Strait. *Deep-Sea Res. (II)* **57**, 1783–1791.

STOMMEL, H. 1965 *The Gulf Stream: a Physical and Dynamical Description*. Cambridge Univesity Press.

STOMMEL, H. 1982 Is the South Pacific helium-3 plume dynamically active? *Earth Planet. Sci. Lett.* **61**, 63–67.

STOMMEL, H. & YOSHIDA, K. 1972 *Kuroshio, Its Physical Aspects*. Univesity of Tokyo Press.

THOM, R. 1972 *Stabilite Structurelle et Morphogenese*. Benjamin.

THOM, R. 1975 *Structural Stability and Morphogenesis*. Benjamin-Addison Wesley (translated by D. H. Fowler).

YUAN, D. & WANG, Z. 2011 Hysteresis and dynamics of a western boundary current flowing by a gap forced by impingement of mesoscale eddies. *J. Phys. Oceanogr.* **41**, 878–888.

https://doi.org/10.1017/jfm.2013.645 Published online by Cambridge University Press